Mechanics of Materials 163 (2021) 104090

Contents lists available at ScienceDirect

Mechanics of Materials

journal homepage: www.elsevier.com/locate/mechmat

Kinematic and thermal characteristic of discontinuous plastic flow in metastable austenitic stainless steels

J. Tabin [a,b]

[a] Institute of Fundamental Technological Research, Polish Academy of Sciences, 02-106, Warsaw, Poland
[b] Institute of Applied Mechanics, Faculty of Mechanical Engineering, Cracow University of Technology, 31-864, Cracow, Poland

ARTICLE INFO

Keywords:
Discontinuous plastic flow
Phase transformation
Macroscopic shear band
Thermomechanical processes
Cryogenic temperatures

ABSTRACT

The strain induced martensitic phase stabilizes the propagation of macroscopic shear band during displacement-controlled uniaxial tensile test of metastable austenitic stainless steels (316 L, 304) at liquid helium temperature (4.2 K). It leads to huge Lüders-type deformation, high hardening and large ductility of the specimen. In Lüders range, shear band develops across the specimen in discontinuous and sequential way, which is reflected by stress oscillation on stress-strain curve and comb-like profile of temperature recorded during tests (so called discontinuous plastic flow - DPF). Based on the time responses of temperature and elongation transducers, a full picture of the localized deformation behaviour of specimen at 4.2 K was obtained, including its both spatial and temporal features. Moreover, the experimental results clarified that DPF has mechanical origin and it is accompanied by thermal effects. The model of temperature distribution during DPF was proposed. The model involves temperature effects driven by the elastocaloric phenomenon (experimentally identified at 4.2 K) and the plastic power dissipation. Based on the model, kinematic and thermal limits of DPF in the austenitic stainless steels were determined.

1. Introduction

Austenitic stainless steels (ASS) exhibit excellent deformability at cryogenic temperatures due to theirs fcc (face-centred cubic) structure, which make them prospective materials for cryogenic industrial applications. It is merely sufficient to point out that the austenitic stainless steel was selected as ITER (International Thermonuclear Experimental Reactor) correction coils case material to provide structural reinforcement to the winding pack (Xin et al., 2017), or according to the latest news, the Starship (the SpaceX's vehicle designed to carry both crew and cargo on long-duration interplanetary flights) will be made of stainless steel rather than carbon fibres, as originally planned (https://www.spacex.com/vehicles/starship/index.html). Nevertheless, unusual tensile behaviours have been observed in a such material at cryogenic temperatures. When temperature tends to the absolute zero, below a transition temperature T_1 (for 316 L reaches 35 K) the discontinuous plastic flow (DPF) occurs (Obst and Nyilas, 1991). This effect, also called a serrated yielding or an intermittent plastic flow, is reflected by the stress oscillation during a displacement-controlled uniaxial tensile test. Moreover, when a yield point is reached, the long stress plateau occurs (for 316 L, 304), which seems a Lüders-type deformation (Fig. 4) - normally observed at room temperatures in carbon steels (Bućko et al., 2014; Hallai and Kyriakides, 2011) or in ultra-fine grained austenitic stainless steels (Gao et al., 2019). Emergence of the stress plateau is related to the strain induced martensitic transformation which stabilizes the discontinuous propagation of the shear bands across the tensile direction. It is worth pointing out that below M_d (the temperature above which the austenite is stable and no martensite is formed by plastic deformation) the phase transformation becomes more intensive (Angel, 1954), and significantly influences the plastic deformation (Tabin et al., 2016). T_1 and M_d parameters are strongly material dependent. Generally, the processes occurring in the austenitic stainless steel at 4.2 K are strictly related to their physical and mechanical properties, e.g. to the type of lattice and its imperfections as well as to the mechanisms of heat transport. For instance, when temperature tends to the absolute zero, a thermal conductivity, a thermal contraction coefficient, and a specific heat also tend to zero. It leads to a thermodynamic instability (Pobell, 2007; Skoczeń et al., 2010) - an arbitrary small dissipation of energy in the lattice will produce a significant increase of temperature (Fig. 7 c). It has fundamental meaning for heat exchange during deformation. The combination of the temperature and strain measurements could provide a knowledge about the spatio-temporal characteristics of the shear

E-mail address: jtabin@ippt.pan.pl.

https://doi.org/10.1016/j.mechmat.2021.104090
Received 29 June 2021; Received in revised form 13 September 2021; Accepted 27 September 2021
Available online 5 October 2021

bands during tension of ASS at cryogenic conditions. It seems crucial when dealing with the tests in the cryostat which is not transparent and does not allow to observe the sample directly.

The objective of this paper is to study the kinematic-thermal aspects of plastic instability behaviours in the austenitic stainless steel (304, 316 L) in the context of existing theoretical hypotheses. The temperature change of specimen recorded during the uniaxial tensile test is used for building an energy balance equation for the displacement-controlled uniaxial tensile test of austenitic stainless steel at 4.2 K. Based on it and the experimental results, the kinematic and thermal limits of DPF in ASS are determined.

There are two basic hypotheses concerning the mechanism of the appearance of DPF, first one based on the dislocation dynamics and the second one related to the thermal effects (Pustovalov, 2008). Basinski (1957) was the first, who attributes the load drops to the thermodynamic properties of materials at very low temperatures. In particular, the author explained the DPF origin by adiabatic heating, based on the assumption that during a sufficiently fast dissipative process at very low temperatures, an increase of temperature and a consequent decrease of the flow stress is observed. It leads to the negative slope of the plastic flow when temperature increases. Starting from the same year, the other authors like Wessel (1957) or Tabachnikova et al. (1984), developed a different approach. The high flow stresses at very low temperatures induce avalanche production of mobile dislocations which may be the origin of the observed serrations. Zaiser and Hähner (1997), in turn, attributed the plastic flow discontinuities at extremely low temperatures to the strain rate softening instabilities. Obst and Nyilas (1991), in their explanation of DPF, made reference to the work by Seeger (1957). In particular, they assumed that in the weakly excited lattice the pile-ups of dislocations are created on the internal barriers and lead to the stress concentrations which may reach the level of the shear strength. Moreover, they assumed that a collective and a catastrophic process of breaking the lattice barriers takes place, leading to the macroscopic shear and the associated drop of stress. This process may be followed by further generation of dislocations, as soon as the obstacles are broken. It is worth pointing out that at 4.2 K the obstacles remain stable because of weakly exited lattice and lack of thermal energy. Therefore, the dynamic strain aging (DSA) as a mechanism of plastic flow instability is ruled out in such conditions (Tabin et al., 2017). A multiscale and coupled model of DPF at cryogenic temperatures has been developed by Skoczeń et al. (2010) and Tabin et al. (2016). However, the broad-based kinematic and thermal characteristics of the plastic deformation of the austenitic stainless steel have been not considered yet. Moreover, despite the large number of experimental observations attesting to the presented hypotheses of DPF, the question about their mechanism still remains open (Pu et al., 2021; Pustovalov, 2008). This study presents the experimental results that confirm the mechanical origin of DPF, as well as the fact that the martensitic phase transformation significantly affects a macroscopic shear band propagation (Tabin et al., 2016, 2019). In the context of second thesis, it is worth recalling the experimental results presented by Shibata et al. (2006, 2008). The Authors identified how the effect of heat, strain and strengthening generated by martensitic transformation influence the behaviour of austenitic stainless steel (ASS) during a uniaxial tensile test at 4.2 K. For this purpose, the Authors tested 310S (ASS stable at cryogenic temperatures), 316 L and 304 L (ASS metastable at cryogenic temperatures). The Lüders-type deformation did not occur only in 310S. Moreover, the ultimate tensile strength and the volume fraction of martensite occurred highest for 304 L compared with others. The Lüders-type deformation in 304 L and 316 L was confirmed at 77 K by Spencer et al. (2009) and Li et al. (2020). Based on the microscopic analysis, it turned out that the shear band consists of 80% martensite in volume fraction while the region far away from a shear band is

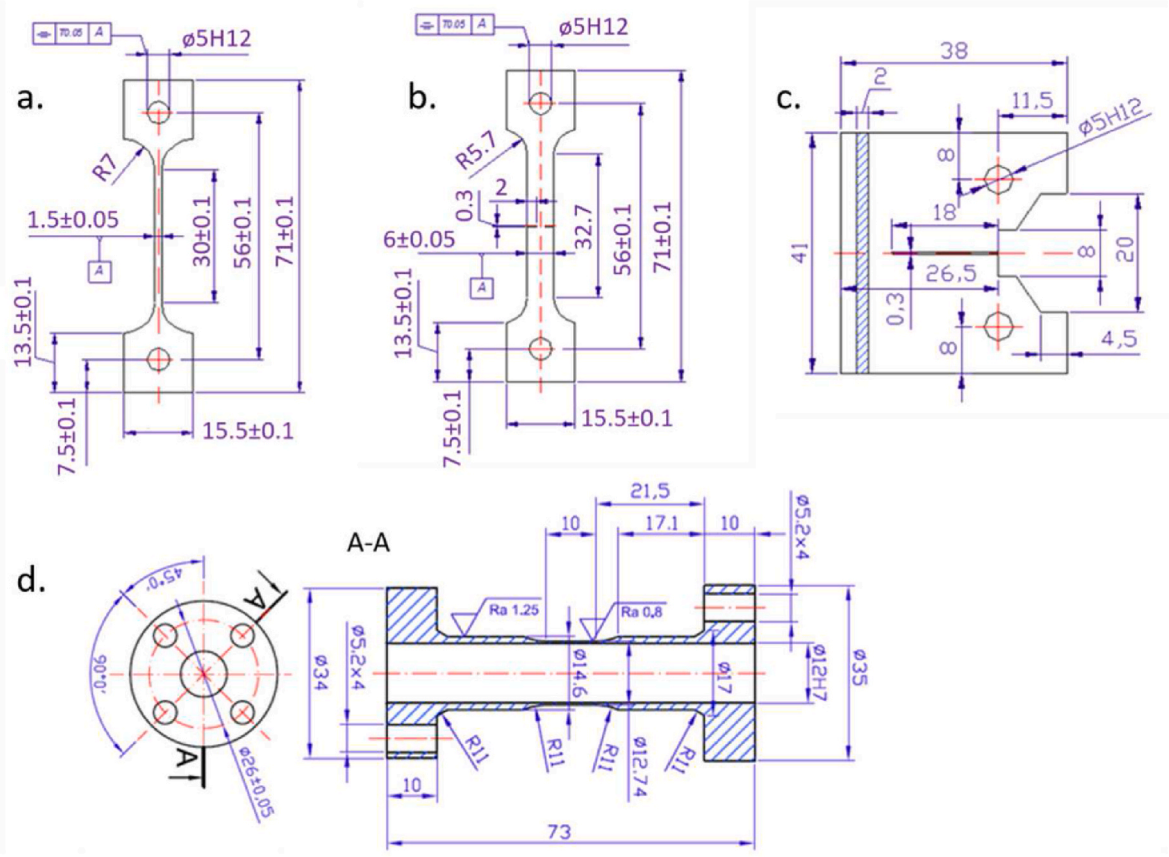

Fig. 1. The specimens used during tests at 4.2 K: a) dog bone specimen (#1), b) specimen with symmetrical notches (#2), c) compact tension specimen (#3) and d) tubular specimen for tension and torsion tests.

composed mainly of austenite. Park et al. (2010) showed that between room temperature and 110 K, the behaviour of ASS was strongly dependent on temperature and strain rate. Based on the experimental results, a viscoplastic damage model was proposed (Kim et al., 2014). Nevertheless, a detailed examination of deformation mechanism was not presented. This issue was considered – among others – by Suzuki et al. (1977) and Brooks et al. (1979a, b). The Authors suggested that the nucleation of α' -martensite is associated with the piling-up of the Shockley partial dislocations on the "stair-rod" dislocation (the Lomer - Cottrell lock). Thus, as the dislocations are forced closer to each other in the pile-up, the atomic structure starts to resemble the bcc stacking. When the pile-up reaches a critical size, rapid growth of the α' -martensite embryo occurs with the aid of the chemical driving force. It appears that the growth of the α' -martensite phase occurs during plastic deformation, through the continuous nucleation and the coalescence of the α' -martensite embryos (Murr et al., 1982).

In addition to the direct transition $\gamma \rightarrow \alpha'$, the three-stage transformation $\gamma \rightarrow \varepsilon \rightarrow \alpha'$ was observed in ASS at cryogenic temperatures. The analysis was carried out by means of the High Resolution Transmission Electron Microscopy (HRTEM) and the atomistic molecular dynamics simulation (Yang et al., 2015). Moreover, the atomic-scale observation showed the lattice orientation relation between γ -austenite, ε - and α' -martensite (Kurdyumov–Sachs or Pitsch orientation relations). On the other hand, Liu and Kaoumi (2018) captured in 304 the formation of stacking faults, as well as the subsequent formation of ε -martensite, confirming the role played by stacking faults as an intermediate step during $\gamma \rightarrow \varepsilon$ transformation. In addition, direct transformation $\gamma \rightarrow \alpha'$ was captured under specific temperature conditions, indicating how deformation and temperature both affect the transformation. Nalepka et al. (2021), in turn, investigated the evolution of the 316 L microstructure in notched specimens at liquid helium. The microscopic analysis of the metastable materials strained at extremely low temperatures showed that the increase of the stress caused more intensive rotation of the austenite grains. At 4.2 K, accommodation of this effect by means of dislocation gliding was difficult. Therefore, inhomogeneous twin shears (i.e. the formation of martensite ε bands) occurred, whose crossing generated the final martensite α'. In this way, rotation of the austenite grains was blocked and only a small part of them reached stable "brass orientation". The mechanism was identified by means of EBSD and X-ray diffraction with the use of synchrotron. Also, it turned out that some fractions of the austenite grains achieved the final "brass orientation" by twinning. Those fractions acted as barriers piling up the dislocations. Breaking them led to DPF, during which the martensite phase might possibly be generated.

Regarding the stable austenitic stainless steels (e.g. 316LN), Han et al. (2018) carried out the in-situ transmission electron microscope (TEM) analysis at 77 K and at 4.2 K. The observations in nanoscale revealed that γ -austenite grains achieved deformation by twinning under low-strain conditions. It means that the deformation of 316LN was mainly achieved by twinning, and in particular, that the twinning was formed prior to the martensite.

The deformation mechanisms during equibiaxial and uniaxial tests of 304 austenitic stainless steels were investigated by Polatidis et al. (2019). During the uniaxial loading, the evolving crystallographic texture favoured the deformation twinning and delayed the martensitic transformation. On the other hand, during equibiaxial loading, the strain was accommodated by shear along multiple shear planes, which provided nucleation sites for martensitic transformation. It means that the deformation mechanism depends on the load path and the deformation texture. It is consistent with the results obtained during tension-torsion of 304 at 4.2 K (Tabin et al., 2021).

Finally, it is worth paying attention to the behaviour of the heterogeneous low C steel/304 austenite stainless steel laminates under tension at 77 K (He et al., 2020). Martensite transformation was concentrated in the localized strain zone of 304 to regain strain hardening ability and reduce severity of the strain concentration. Thus, the non-uniform martensite transformation along the gauge length was the origin of the strain delocalization in the localized strain zone.

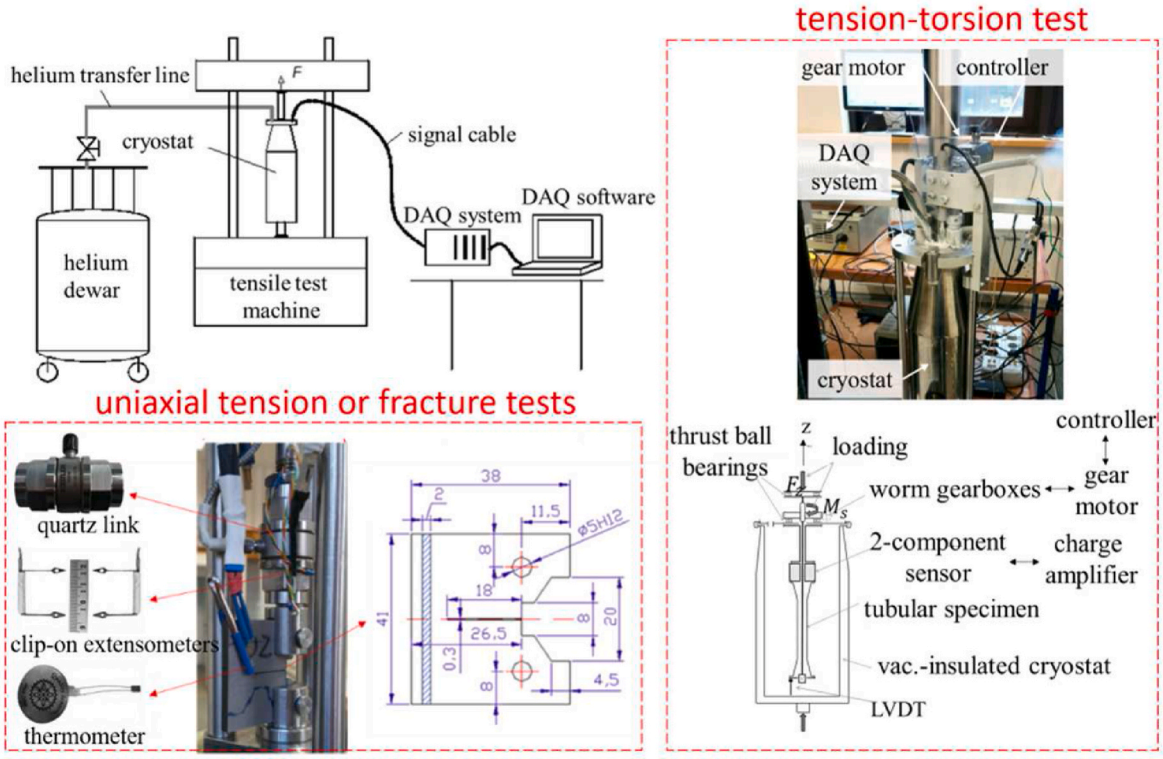

Fig. 2. In-house experimental set-up for tests at 4.2 K: cryostat equipped with suitable instrumentation (quartz link, clip-on extensometers, thermometer, specimens) and mounted in the test machine; transducers are connected to DAQ system.

2. Materials and experiments

In the present study the austenitic stainless steel (316 L or 304) was examined. The chemical compositions of the tested specimens are listed in Table 1.

Displacement-controlled tests were conducted at liquid helium temperature (4.2 K), at liquid nitrogen temperature (77 K) and at room temperature. In order to identify the kinematic and thermal aspects of discontinuous plastic flow different types of specimens and loading were used (Figs. 1 and 2).

The specimens were fabricated by means of the electrical discharge machining (EDM) from a commercial stainless steel sheet and bar with the tensile axis in the rolling direction. The semi-products were supplied in the annealed and lightly cold-rolled conditions (according to the standard ASTM A480 and EN 10,088). In a such form the materials are typically used for the structural components working at cryogenic conditions, down to the temperature of superfluid helium, 1.9 K (Bertinelli et al., 2006).

The mechanical testing at extremely low temperatures implies use of the specific cryogenic devices (Fig. 2). The heart of the system remains the cryostat (vacuum insulated enclosure around the sample), connected to the liquid helium dewar by means of the helium transfer line. Before starting any tests, the liquid helium flows from the dewar to the cryostat, until the specimen equipped with the sensors is immersed in the cryogenic medium. The cryostat is mounted between the grips of the tensile test machine which performs displacement-controlled tension or tension and torsion (Fig. 2). The stiffness of the testing machine influences the plastic flow instability (Vorob'ev, 2006), therefore, the tests are performed by means of very stiff Instron TT. The piezoelectric force transducer for highly dynamic measurements is mounted in the cryostat, just behind the specimen. The transducer is calibrated in li quid helium. The reference force measurements are carried out by the external load cell.

The light-weight clip-on extensometers, which are designed for the tensile test at cryogenic temperatures, are attached directly to the specimen (Tabin and Prącik, 2015). To hold the extensometers, two bronze springs are used. In order to monitor the temperature of the specimen, the thin film resistance cryogenic temperatures sensors (Lakeshore Cernox SD) are fixed directly to the specimen. The sensor is characterized by fast thermal response times: 1.5 ms at 4.2 K, 50 ms at 77 K. The thermometers are calibrated at liquid helium temperature. The thermal grease is selectively used to install and fasten the sensors to the specimen, providing a thermal contact and an electrical insulation. The time responses of the transducers are recorded at the sampling rate of 1 *kHz*. The general tensile test parameters are presented in Table 2.

The DPF is a dissipative process during which a heat generation occurs (Fig. 5 c, b). The heat transport in the lattice at cryogenic temperatures is essentially represented by two mechanisms: the phonons and the free electrons (Pobell, 2007). Macroscopically, heat transfer occurs in three basic ways: a conductive heat transfer through specimen, a convection through cryogenic medium and a radiation. It is worth pointing out that in the proximity of absolute zero several thermodynamic parameters (e.g. a thermal conductivity and a thermal contraction coefficient) or state functions (e.g. a specific heat and an entropy) tend to zero. The background of thermodynamic of processes in metals and alloys at near 0 K is presented by Skoczeń (2004, 2010).

Based on the literature data (Bauer et al., 2007; Marquardt et al., 2000; Rossi and Sorbi, 2006) the estimates of the specific heat and the thermal conductivity for fcc materials (304 and OFE Cu) are obtained in a wide range of temperatures (4 K–300 K, Fig. 3).

The specific heat C_v and the thermal conductivity k for 304 austenitic stainless steel are non-linear functions of temperature (Marquardt et al., 2000):

$$\log k = -1.4087 + 1.3982 \log T + 0.2543(\log T)^2 - 0.6260(\log T)^3 + 0.2334(\log T)^4 + 0.4256(\log T)^5 - 0.4658(\log T)^6 + 0.1650(\log T)^7 - 0.0199(\log T)^8 \quad (1)$$

$$\log C_v = 22.0061 - 127.5528 \log T + 303.6470(\log T)^2 - 381.0098(\log T)^3 + 274.0328(\log T)^4 - 112.9212(\log T)^5 + 24.7593(\log T)^6 - 2.239153(\log T)^7$$

The experimental data show that below 100 K, the specific heat approximately decreases exponentially in the austenitic steel (Fig. 3 b). At very low temperatures, below 10 K, the specific heat becomes linear and according to the third law of thermodynamics - tends to zero.

As the thermodynamic functions tend to 0 with temperature, the so called thermodynamic instability takes place (Skoczeń et al., 2010):

$$\frac{dT}{dQ} \xrightarrow{T \to 0} \infty \quad (2)$$

This means that in the proximity of absolute zero an arbitrary small dissipation of energy *dQ* in the lattice will produce significant increase of temperature dT. Among possible sources of energy dissipation at cryogenic temperatures, such processes like an inelastic deformation has to be accounted for. In particular, a plastic deformation represented by a massive motion of dislocations in the lattice or by a localized effect in the form of macroscopic shear bands will produce enough energy to raise the temperature of specimen by several Kelvins. Figs. 5 c, Fig. 7 c and 8 (a) present an example of thermodynamic instability during displacement-controlled uniaxial tensile test at 4.2 K.

3. Results

3.1. Plastic flow instability at cryogenic temperatures

The displacement-controlled uniaxial tensile tests of 316 L specimen (#1) were carried out at different temperatures: 4.2 K, 77 K and at 293 K (room temperature). The stress-strain curves are presented in Fig. 4.

It should be noted that the deformation behaviour of 316 L dog bone specimen at cryogenic temperatures is remarkably different from that at room temperature. The yielding behaviour transits from the typical continuous plastic flow in room temperature and 77 K to the discontinuous plastic flow (DPF) at 4.2 K, reflected by the stress oscillations. The stress plateau suggests the Lüders-type deformation at cryogenic temperatures (cf. Spencer et al., 2009). The Lüders elongation is less

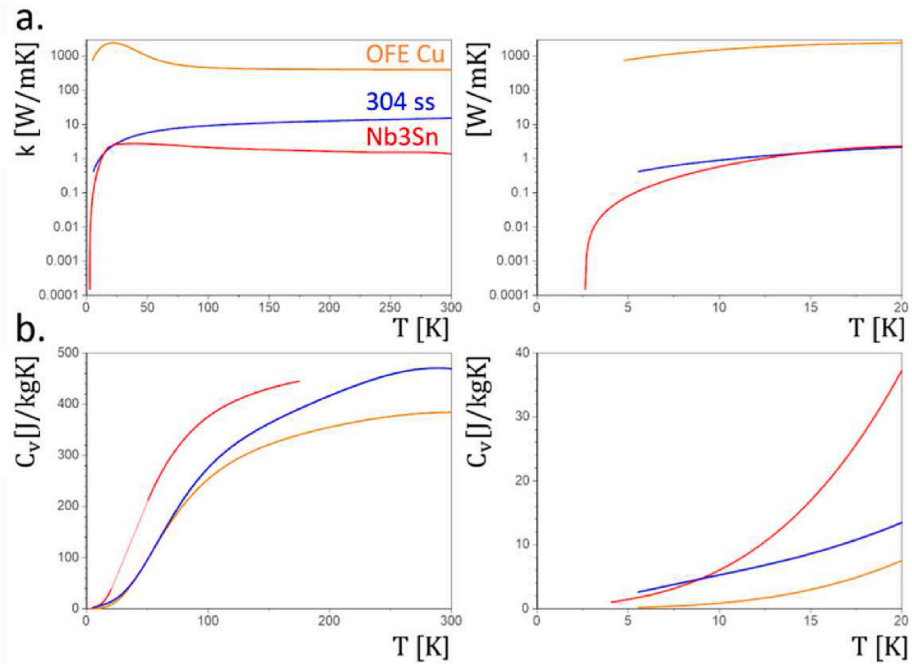

Fig. 3. Thermal conductivity k and specific heat C_v as a function of temperature for 304 austenitic stainless steel (blue), OFE Cu (orange), and Nb3Sn (red) (Marquardt et al., 2000). (For interpretation of the references to colour in this figure legend, the reader is referred to the Web version of this article.)

than half of the total elongation. After the stress plateau, the strain hardening occurs. It is worth pointing out that during plastic deformation at cryogenic temperatures the strain induced phase transformation in ASS is significantly more intensive and starts earlier then at room temperature (Angel, 1954). Therefore, the strain hardening is higher at cryogenic temperatures than at room temperature (cf. Fig. 4).

Digital Image Correlation (DIC) and Infrared method (IR) are a vision-based data acquisition system which fully captures a field deformation, a strain and a temperature almost only at room temperature (Jin et al., 2021). The experimental set-up for a test at cryogenic temperatures consists of the cryostat (Fig. 2) which is not transparent, therefore does not allow to observe the sample directly. Only the time responses of transducers can by analysed. The initial study of the strain localization during displacement-controlled tensile test of stainless steels at 4.2 K is presented by Tabin et al. (2016). However, this effect needs detailed explanation in context of kinematic and thermal characteristic of the shear band during DPF. Thus, the temperature distribution and the time response of extensometers indicate the inhomogeneity in the deformation behaviour of the specimen during the uniaxial tensile test at 4.2 K. The elastic deformation (stage I on Fig. 5) takes place as long as the yield stress is achieved. Due to the fact that the plastic deformation can occur beyond the extensometer's range (Fig. 5 h), the nonlinear range of classical plastic flow is observed (stage II) together with the slight increase of the specimen's temperature (Fig. 5 c). Then, the first serration occurs, reflected by the abrupt drop of the stress. During stage IIa, the shear band fully develops and penetrates across the gauge length of the specimen (Fig. 5 d). Sequential and discontinuous propagation is confirmed by the stepwise increase of the elongation signal and the comb-like profile of temperature (Fig. 5 f, c, respectively). In order to reduce the influence of the specimen's shape on the temperature measurements, the time responses of temperature sensors are divided by the maximum temperature recorded during the test (e.g. for 316 L $\Delta T_{max} = 35$ K). The elongation plateau occurs after the shear band reaches the end of the extensometer's gauge length (Fig. 5 e, g). Than the squeezing of extensometer's arms and the drop of elongation signal are observed (Fig. 5 g). It takes place until one of the specimen's shoulders is reached by the shear band. Then, the shear band starts to propagate in a random way. The regular form of the temperature distribution is not further observed, and the time response of extensometers shows occasionally a drop of signal. This stage (III) takes

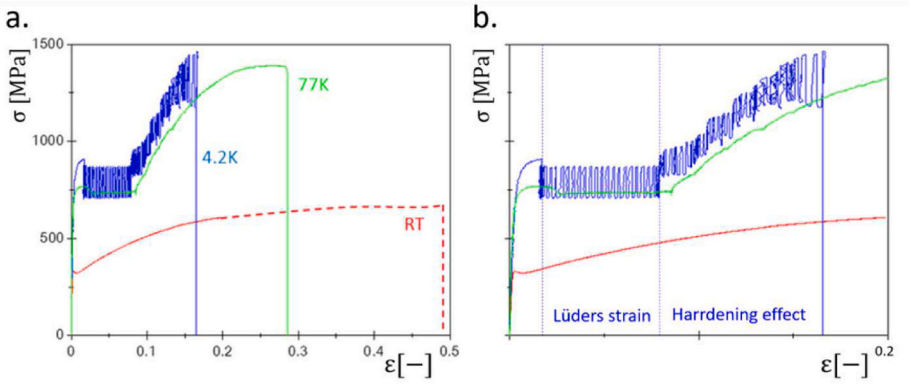

Fig. 4. a), b) Tensile tests results: the stress - strain curve for 316 L stainless steel at liquid helium temperature (4.2 K), at liquid nitrogen (77 K) and at room temperature (RT); b) tensile test results for the strain threshold $\varepsilon = 0.2$.

place until a rupture of the specimen occurs. It is worth pointing out that similar deformation behaviour was observed during the uniaxial tensile test in the ultra-fine grained austenitic stainless steel fabricated by two-step cold rolling and annealing process (Gao et al., 2019). The Authors demonstrate the role of strain induced martensitic transformation in deformation behaviour. Namely, the new phase stabilizes the propagation of the shear band, leading to the huge Lüders-type deformation, the high hardening and the large ductility of the material.

In order to clarify the spatio-temporal characteristic of plastic deformation, the extra test was carried out. The experimental set-up is presented in Fig. 7 a. During the displacement-controlled uniaxial tensile test two thermometers are used. One of them is mounted near the lower shoulder of the specimen (green), the second one in the central part of the specimen (blue).

Fig. 7 b and d contain, respectively, the time responses of quartz link and thermometers. The elastic stage (I) is observed until the increase of the specimen temperature occurred (blue curve, Fig. 7 c). Then the

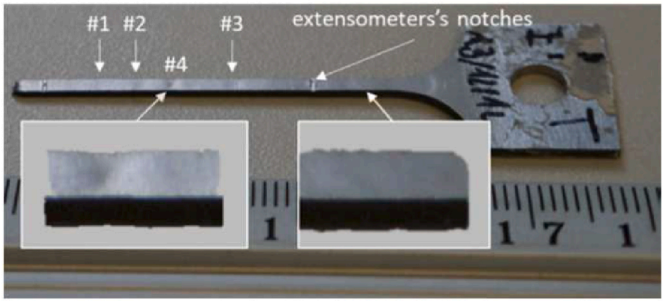

Fig. 6. Multiple necking pattern (1–4) in 316 L during displacement-controlled tensile test at 4.2 K.

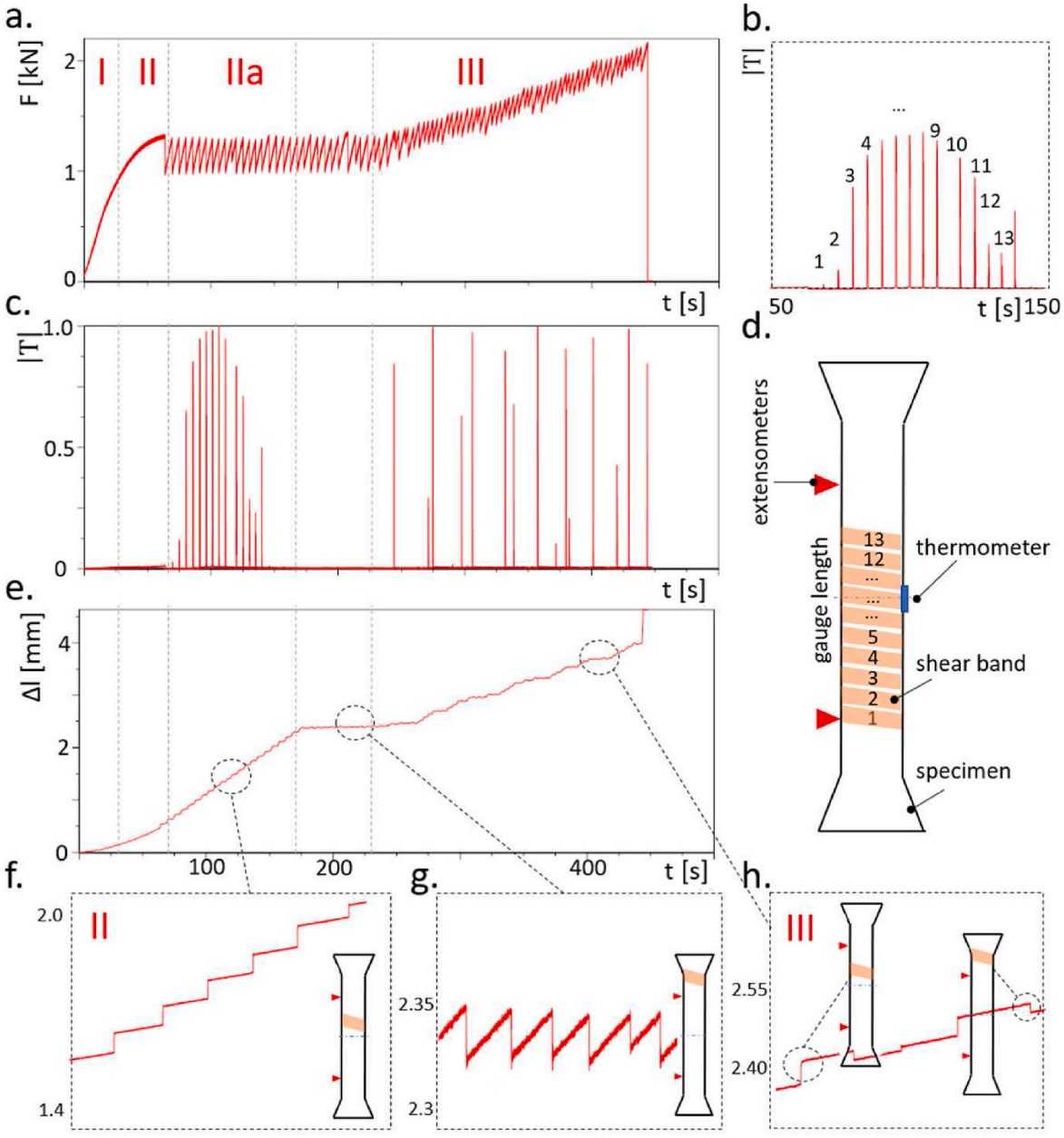

Fig. 5. Time responses of transducers during uniaxial tension of 316 L at 4.2 K: a) quartz link (F), (e, f, g, h) extensometers (Δl) and (b, c) thermometer $|T|$ (normalized value); d) illustration of shear band development across the specimen (stage IIa).

nonlinear continuous plastic flow takes place with monotonic increase of temperature up to the first drop of the stress (stage II). This serration is reflected by the peak of the temperature signal (blue curve). It means that the shear band occurs near to the upper shoulder of the specimen and the dissipated heat is so significant that it excites the blue thermometer. It confirms the thesis that the shear band is triggered due to the stress concentration effect (in the previous test the initiation of shear band occurred under knife edge of extensometer, Fig. 6). Then the shear band is switched to the lower shoulder of the specimen (simultaneous effort of specimen's shoulders) and propagates in the sequential and discontinuous way (stage IIa). In this stage the strain-induced phase transformation stabilizes the propagation of the shear band, leading to the huge Lüders-type strain. Then the strain hardening effect is observed (stage III, cf. Fig. 4). The time responses from thermometers indicate that the shear band in stage III occurs randomly along the specimen (Fig. 7 d). In the period between 20 and 35 s, there are no recorded temperature spikes because the shear band holds the position beyond the sensing range of the temperature sensor.

The strong strain localization induces the intensive phase transformation, however for the high-volume fraction of the martensite, the deformation is blocked, and the shear band is switched to another place (strain delocalization). Therefore, the multiple necking pattern is commonly observed after the test (Fig. 6).

In order to summarise the deformation behaviour of 316 L metastable austenitic stainless steel with the strain induced phase transformation during the kineamtically-controlled uniaxial tensile test at 4.2 K, the evolution of the shear band and the martensitic phase are schematically presented in Fig. 7 e.

The scheme explains the stabilization effect of the strain induced martensitic transformation on the Lüders-type elongation.

3.2. Experimental identification of DPF mechanism

There are two basic hypotheses concerning the mechanism of DPF, first one based on the dislocation dynamics and the second one related to the thermal effects. There exist numerous experimental observations attesting to both hypotheses, however the question about the mechanism of DPF remained open until now (Pu et al., 2021; Pustovalov, 2008). In order to clarify these hypotheses during the uniaxial tensile test at 4.2 K, the quartz link and the thermistors are used to measure, respectively, the applied force and the specimen's temperature. When the comb-like profile of temperature is initiated (the shear band approached the measurement's zone of thermometer), the test is interrupted, and the specimen is unloaded. Then, the specimen is loaded again, and the displacement-controlled test is continued. The time responses of the transducers are presented in Fig. 8 a. The results show that after resuming, the comb-like distribution of temperature is preserved, even though the specimen achieved the liquid helium temperature. It means that the development of the shear band is maintained, obviously, still in the discontinuous and the sequential manner. In other words, the specimen's microstructure has a memory of loading history.

During the next test, the displacement-controlled uniaxial tensile test is interrupted and resumed after 15 s (Fig. 8 b). When the specimen is reloaded, the profile of serration is still preserved. It means that the pile-ups of dislocation on the internal lattice barriers are maintained despite of test interruption. When the stress achieved the level of the shear strength, abrupt drop is observed (Fig. 8 b).

Each serration in the stress-strain curve shows similar pattern (Fig. 9 c): after elastic range (1), smooth plastic flow occurs (2) up to abrupt drop of the stress (3) and further relaxation (4). Moreover, each stage is accompanied by a considerable local changing of temperature, related to

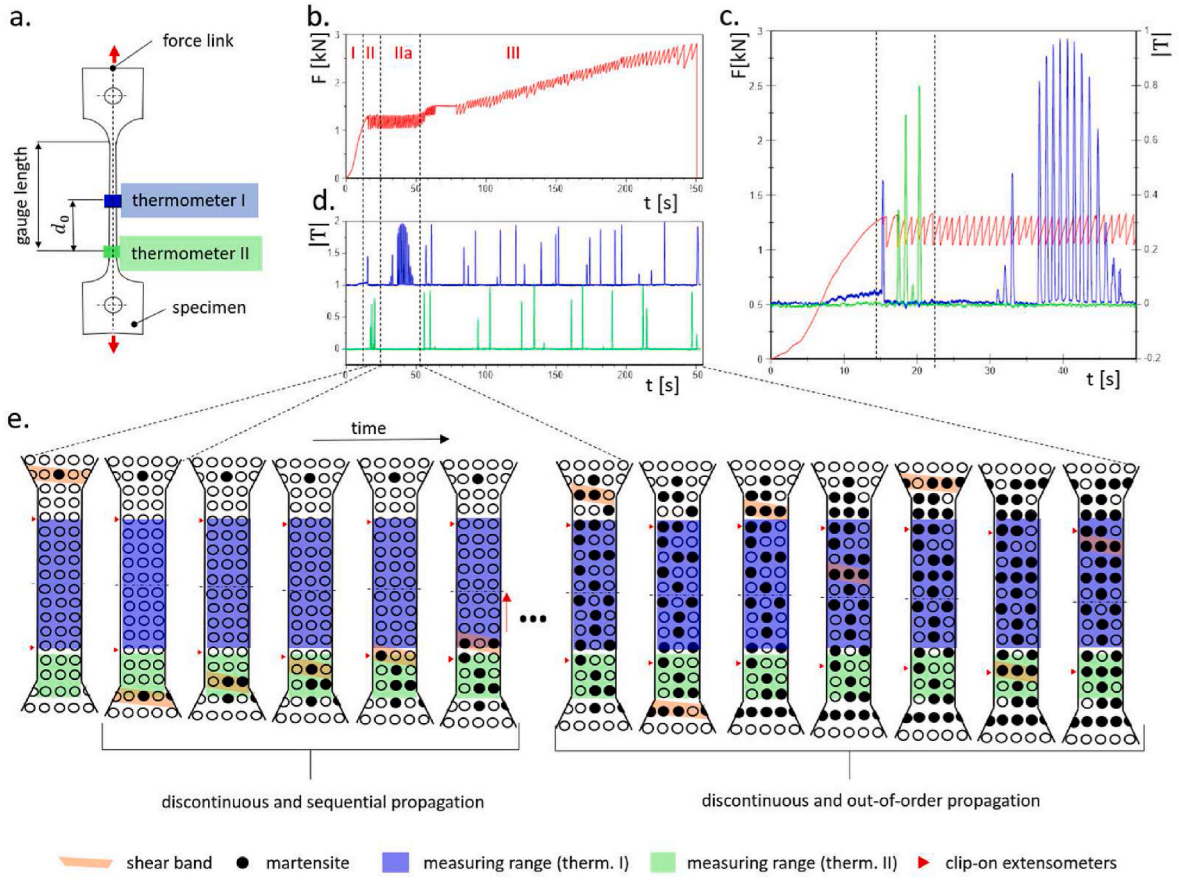

Fig. 7. a) Experimental set-up for tracing the shear band propagation during uniaxial tensile test at 4.2 K; time responses of b) quartz link (F) and (c, d) thermometers $|T|$ (normalized value); e) illustration of strain induced behaviour of 316 L specimen.

Table 1
Chemical composition of specimens.

	Chemical composition %							
	C	Si	Mn	P	S	Cr	Ni	N
316 L	≤0.030	1.00	2.00	0.045	0.015	18.200	11.500	–
304	0.07	≤0.8	≤2.0	0.045	0.03	17–19	9–11	

Table 2
Experimental conditions: test parameters and materials properties.

Type of test:	displacement-controlled tension and tension-torsion	
Temperature [K]:	4.2, 77, RT	
Crosshead velocity [mm/min]:	1.0, 2.0 and 100	
Sampling frequency [Hz]:	1000	
Materials:	316 L	304
Proof stress [MPa]:	880	550
Tensile strength [MPa]:	1450	1700
Percentage elongation after fracture [%]:	25	20

the elastocaloric effect and the plastic power dissipation (Fig. 9 b) under the vanishing specific heat and the thermal conductivity (Fig. 3). The simple illustration of the thermomechanical interpretation of the one dimension DPF is presented in Fig. 9 (a), where E_0, μ_0, μ_{serr} are, respectively, a spring constant, a friction coefficient between block and base, a friction coefficient of the clutch. The elastic deformation of the spring reflects the stage 1 of the DPF serration. Then, the sliding block describes the stage 2. Finally, the discontinuous sliding of the clutch represents the stage 3. Each of the stages is related to the heat dissipation or the absorption (Fig. 9 a). The detailed description and definitions of the heat sources are presented in section 3.4.

During the displacement-controlled quasi-static tensile test at 4.2 K the failure of lattice barriers is reflected by the macroscopic shear $\Delta\varepsilon_p^{serr}$ (Fig. 9 d and e). This shear leads to the unloading of the part of the specimen in quasi-static conditions, therefore the abrupt drop of the stress is observed. It means that the test conditions (e.g. stiffness of tensile test machine, the specimen geometry) may influence the stage 3 of the serration (Vorob'ev and Anpilogova, 2013).

Finally, the experimental results show that the rapture of the specimen takes place in the DPF manner - the serration pattern is maintained. Fig. 10 presents the last serration during the kineamtically-controlled tests of the dog bone specimen (Fig. 10 a), the specimen with symmetrical notches (Fig. 10 b) and the tubular specimen during combined loading - tension and torsion (Fig. 10 c). All the presented results show that the serration mode was maintained during the rapture. It means that in order to describe the fracture mechanism during tension at liquid helium temperature, the DPF mechanism should be considered.

In order to clarify this thesis, the strain localization in austenitic stainless steel was investigated during a fracture test at liquid helium temperature. Fig. 11 shows force versus crack opening displacement (COD) curves for 316 L CT specimen (Fig. 1 c) under displacement-controlled test at 4.2 K and at room temperature. The first four stages in Fig. 11 (a) and c are related to the plastic deformation near the tip of the crack and no crack propagation occurs. Then, the global drop of the force is observed. It results from the crack propagation (stages 5, 6) in the manner imposed by displacement-controlled tensile test.

The similar test was prepared at 4.2 K. The initiation of the plastic deformation and the crack propagation are observed at different points on the force-COD curve. Moreover, the force oscillations related to the DPF occurs at cryogenic temperature. It is worth pointing out, that in the range where the force decreases, the oscillations still occur, corresponding to the DPF-induced crack jumps (green curve on Fig. 12, arrow 1), moreover the shear bands can be blocked in the crack tip area flipping up and down along loading direction (arrow 2). The last effect is observed by Ren et al. (2021) in C–Mn steel notched specimen during test at elevated temperatures where a plastic flow instability related to Lüders and PLC effects occurs.

Finally, the micro-serrations included in macro-serrations (Fig. 12) can be related to a deformation twinning (arrow 3). Such an effect is confirmed by investigations carried out by Obst and Nyilas (1998). However, an important question arises: how much the sample deforms at 4.2 K by twinning, by martensitic transformation, or by dislocation glide, unfortunately the question is still open.

3.3. Kinematic aspects of DPF

Based on the time responses of the transducers, a full picture of the localized deformation of specimen is obtained, including its both spatial and temporal features in stages II and IIa during uniaxial tensile test at 4.2 K (section 3.1). It is demonstrated that the shear band normally initiate due to the stress concentration (e.g. at one of the specimen shoulders) and then propagates along the specimen. The sequential and discontinuous development of shear band in Lüders range is maintained by the strain induced martensitic transformation. Thus, the stress plateau is observed on stress-strain curve. An experimental identification of kinematic parameters of the shear band in the metastable austenitic steels during deformation at 4.2 K is absent in the literature. In order to clarify this, the experimental set-up is changed over to the configuration enables the identification the shear band velocity V_{SB} during tension (Fig. 7 a). Knowing the distance between the two thermometers and the time between the shear band occurring under the

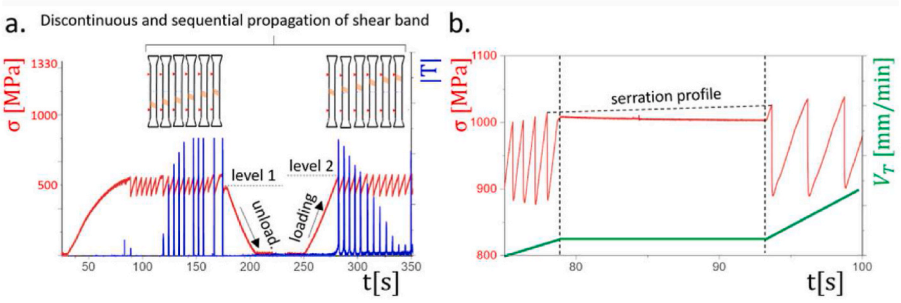

Fig. 8. Displacement-controlled tensile tests of the dog bone specimen at 4.2 K, a) the comb-like distribution of temperature T (blue curve) during loading-unloading event reflects the mode of shear band propagation; b) although the stroke of the test machine actuator V_T is suspended for 15 s, the profile of serration is maintained. (For interpretation of the references to colour in this figure legend, the reader is referred to the Web version of this article.)

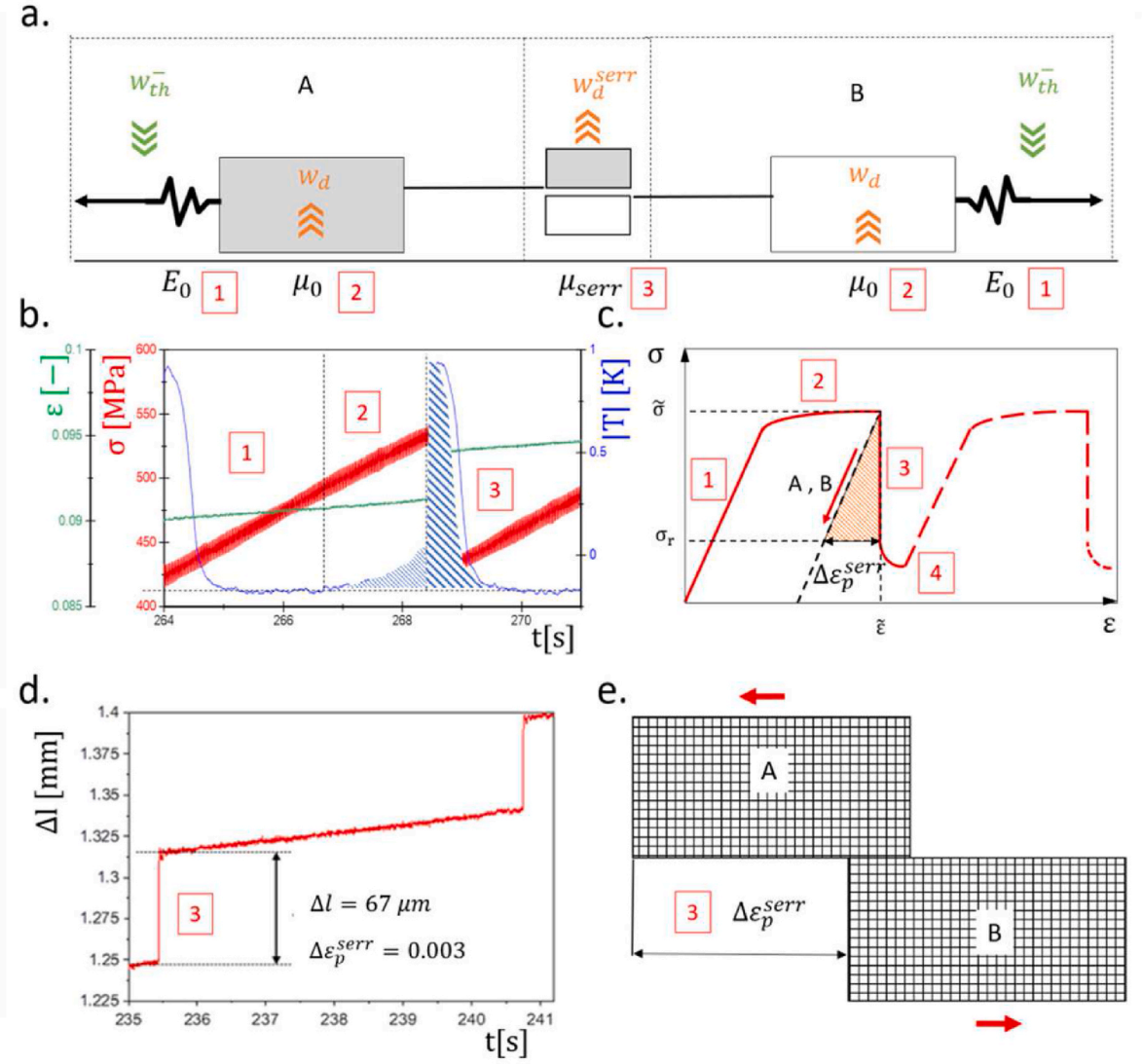

Fig. 9. Single serration during DPF in austenitic stainless steel (304); a) simplified model of serrations (Skoczeń, 2004); energy balance during single serration (cf. section 3.4): w_{th}^- - isentropic energy from the thermoelastic couplings (stage 1), w_d - dissipated energy during plastic deformation (stage 2), w_d^{serr} - dissipated energy during abrupt drop of the stress (stage 3), b) stress σ (red), temperature $|T|$ (blue) and strain ε (green) curves in time domain, c) based on it, the single serration can be identified, where the abrupt drop of the stress (stage 3) in serration is related to macroscopic shear $\Delta\varepsilon_p^{serr}$ in specimen d), e). (For interpretation of the references to colour in this figure legend, the reader is referred to the Web version of this article.)

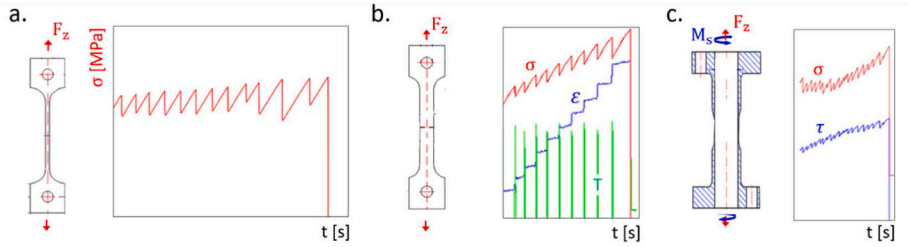

Fig. 10. The last serration during DPF in 304 stainless steel tested at 4.2 K; axial stress (σ), shear stress (τ), strain (ε) and temperature (T) in time domain; a) dog bone tensile test specimen, b) specimen with symmetrical notches and c) tubular specimen for combined loading - tension and torsion (Fig. 1 d).

lower thermometer and then under the centred one, the average velocity is calculated (Table 3).

The experimental results presented in Table 3 are illustrated in Fig. 13 and compared with the experimental data obtained for 0.036% C steel wire and niobium microalloyed steel band tested at room temperature.

The results reveal that the shear band velocity in Lüders range depends on the materials composition, microstructure, specimens thickness and test conditions, such as a velocity of the test machine actuator (Cai et al., 2016) or the test temperature.

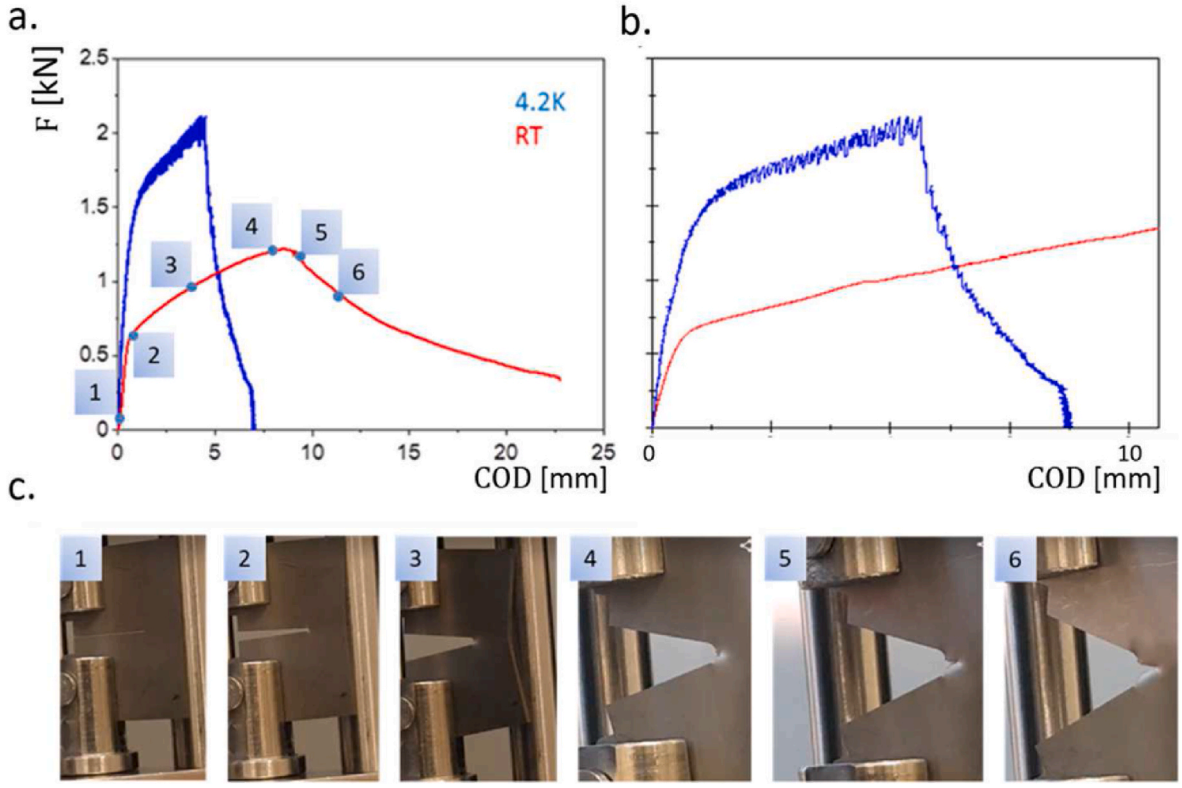

Fig. 11. a), b) Force versus crack opening displacement of 316 L CT specimen at 4.2 K (blue) and at room temperature (red), c) crack propagation during displacement-controlled test at room temperature. (For interpretation of the references to colour in this figure legend, the reader is referred to the Web version of this article.)

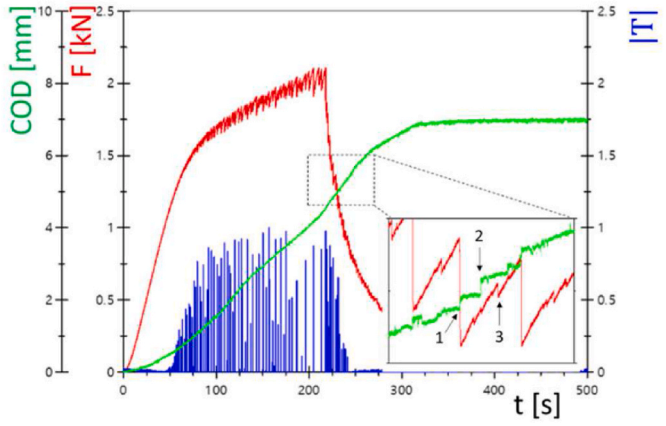

Fig. 12. Crack instability in CT 316 L specimen during DPF conditions at 4.2 K; time responses of transducers: force F (red), crack opening displacement COD (green) and temperature $|T|$ (blue, normalized value). (For interpretation of the references to colour in this figure legend, the reader is referred to the Web version of this article.)

Table 3
Shear band velocity during uniaxial tensile test of dog bone specimen (#1) at 4.2 K

	Gauge length strain rate [1/s]	Shear band velocity [mm/min]
304	0.0026	44.4
	0.0010	13.3
	0.0005	10.6
316 L	0.0010	17.5

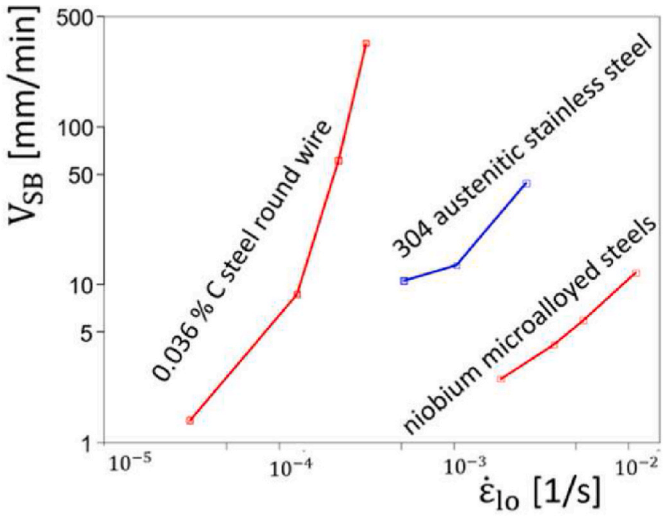

Fig. 13. Shear band velocity (V_{SB}) against gauge length strain rate ($\dot{\varepsilon}_{lo}$) during uniaxial tensile test of: niobium microalloyed steel (Rešković et al., 2016) and steel round wire $\varphi = 1.6\,mm$ (Sun et al., 2003) at room temperature, and 304 austenitic stainless steel (blue) at liquid helium temperature (1.0 mm × 1.5 mm). (For interpretation of the references to colour in this figure legend, the reader is referred to the Web version of this article.)

3.4. Thermal aspects of DPF

The thermomechanical aspects of the strain localization in the austenitic stainless steels at extremely low temperatures, near zero Kelvin, have been partly recognized. An interesting analysis, leading to the better understanding of the mechanism of the DPF, can be found in

Table 4
Loading conditions.

Controlled displacement V_T [mm/min]	Loading Period [s]	Suspension Period [s]	Unloading Period [s]
0.5	0–103	103–116	116–185

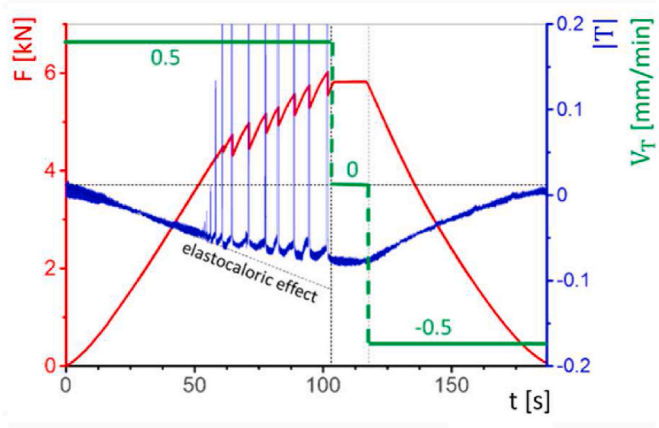

Fig. 14. Elastocaloric effect during uniaxial tensile test of 316 L (specimen #2) with the displacement-controlled mode (V_T) at 4.2 K; time responses of force transducer F (red) and temperature sensor T (blue, normalized value). (For interpretation of the references to colour in this figure legend, the reader is referred to the Web version of this article.)

Vorob'ev and Anpilogova (2013, 2015). The energy balance and the mechanism of plastic flow instability at extremely low temperatures in metals are discussed by the Authors. In particular, the energy of strain jump is analysed. It is shown that most of the potential strain energy is converted to the work. The investigation shows that the strain jump significantly depends on the parameters of the loading system, as well as on the level of material strength. On the other hand, Skoczeń et al. (2014) and Tabin et al. (2016) proposed the thermomechanical model of the DPF in fcc materials. A physically based constitutive model describes both the serrations and the temperature distribution. However, this analysis does not consider the impact of the strain rate and the elastocaloric effect on the temperature distribution during the test of austenitic stainless steels at 4.2 K. The last-mentioned effect is identified during the uniaxial tensile test of 304 specimen with the symmetrical notches (Fig. 1 b). The test is conducted with the displacement-controlled mode at 4.2 K. The loading conditions are listed in Table 4.

The thermal grease is used to connect the thermometer with the sample, providing the thermal contact and the electrical insulation. The thermometer is mounted above the notches. Plastic deformation zone is limited to the notches area. The loading path is schematically illustrated in Fig. 14 (green), together with the time responses of the force transducer (red) and the thermometer (blue). Immediately after loading is applied, the temperature of the specimen decreases. This is how the elastocaloric effect can be observed during tension (Oliferuk et al., 2012).

The thermometer is spaced quite far from the notches (out of the plastic deformation zone), therefore the linear trend of the temperature is observed until the suspension period occurs. After this, during the unloading period, the temperature increases to liquid helium temperature. The DPF manifests by oscillations of the force in the time domain and the Dirac-like temperature distribution (temperature peaks).

The elastocaloric effect is also identified during the test with higher strain rate. The displacement-controlled uniaxial tensile test of 304 (specimen #2) was carried out at 4.2 K, but this time, the velocity of the test machine actuator was $100 mm/\mathrm{min}$. The test results are presented in Fig. 15 a. Immediately after loading is applied, the temperature of the specimen decreases (elastocaloric effect), then suddenly increases due to

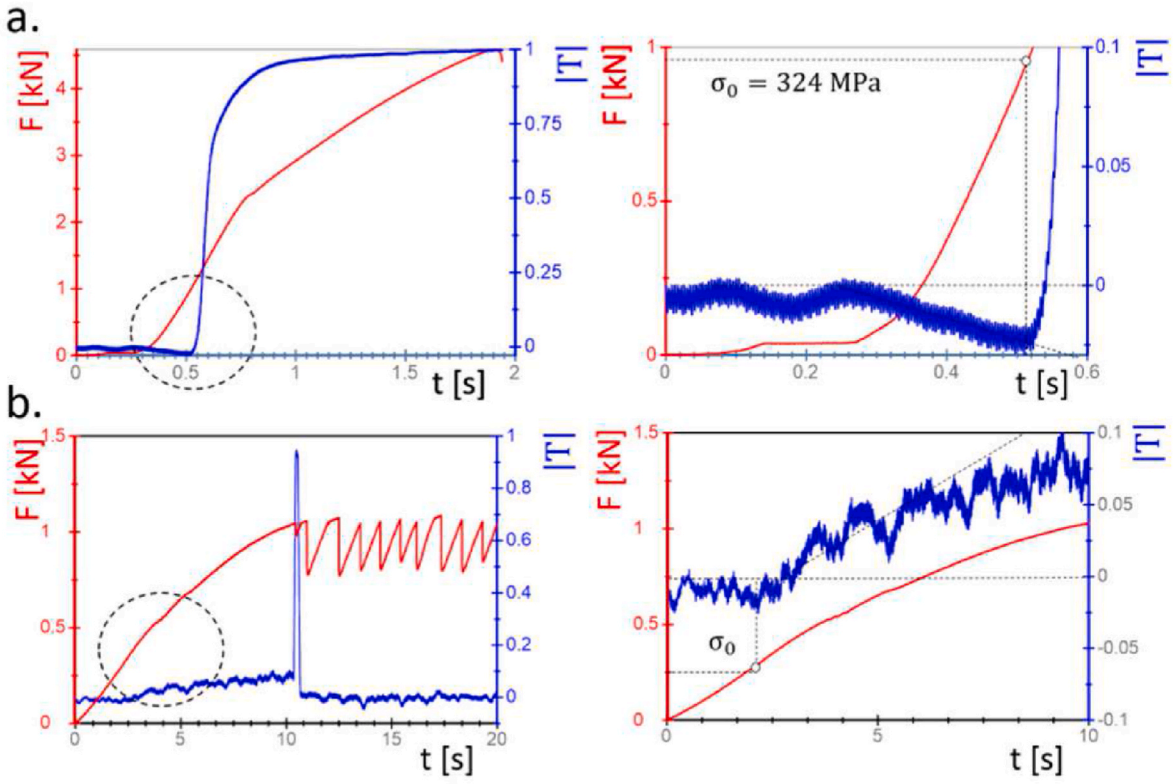

Fig. 15. Elastocaloric effect and microplasticity during displacement-controlled uniaxial tensile test at 4.2 K of: a) 304 (specimen #2) with test machine actuator velocity of 100 mm/min; b) 316 L (#1) with test machine actuator velocity of 1 mm/min.

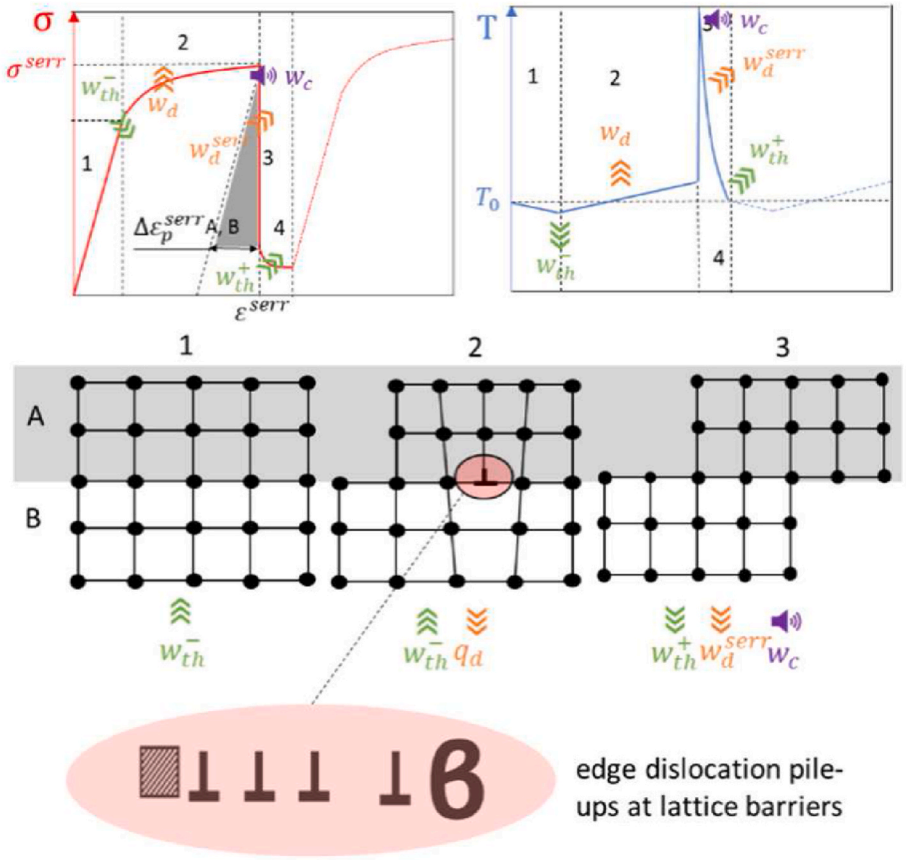

Fig. 16. Decomposition of deformation energy during the DPF. The mechanism of plastic flow instability: massive collapse of lattice barriers at the heads of dislocation pile-ups.

the intensive heat dissipation coming from microplastic effects. During the test, the DPF does not occur, since the temperature of the specimen reached the transition temperature T_1 at the beginning.

It seems that the values of the yield point determined from the thermomechanical coupling are lower than these obtained from the standard test (Oliferuk et al., 2012). The experimental results show that heat dissipation occurs long before the nonlinear response of the force transducer (Fig. 15).

The deformation processes almost always modify the temperature field of the strained material. The presented study of the thermomechanical coupling during the DPF is aimed at modelling the temperature distribution during the displacement-controlled uniaxial tensile test at 4.2 K. Therefore, for the RVE (Representative Volume Element) of elasto-plastic material, a deformation energy w_{ext} can be decomposed into an elastic part (reversible) w_e and a complementary part w_a, which can be further decomposed into a dissipated energy w_d, a stored energy w_s, and an acoustic emission energy of 'dry sounds' w_c, emitted by the specimen when the avalanche-like barriers are crossed by dislocation pile-ups:

$$w_{ext} = w_e + w_d + w_s + w_c \tag{3}$$

This decomposition of the deformation energy during single serration is illustrated in Fig. 16.

The supplementary term w_{th} appears in the elastic loading (w_{th}^-) and in the abrupt drop of the stress (w_{th}^+) (Fig. 16). It is so-called the isentropic energy and comes from the thermoelastic couplings. This heat supply is associated to the temperature variations of the material when transformation is reversible and adiabatic (isentropic) (Chrysochoos and Martin, 1989). In the presented case, it is assumed that the latent heat from the phase transformation is neglected. It means that the dissipation and the isentropic power are both mechanical heat sources included in the heat conduction equation:

$$\rho C_v d(\Delta\dot{T}) - \lambda\left(\frac{d^2(\Delta T)}{dx^2}\right)\Delta T = \eta\sigma\dot{\varepsilon}^p - \alpha E_0 T_0 \dot{\varepsilon}^e \tag{4}$$

where the specific heat is C_v, ρ is the density, E_0 is the elastic modulus, λ denotes coefficient of conductivity, α is the coefficient of thermal expansion, η denotes Taylor - Quinney coefficient and $\Delta T = T - T_0$, where $T_0 = 4.2$ K. It is assumed that the acoustic emission of the DPF does not generate the heat.

The change in the temperature of the material during the elastic deformation is caused by the mutual conversion of the potential and kinetic energy of lattice atoms and can be explained within the framework of linear thermodynamics. During the adiabatic uniaxial elastic deformation, under the assumption of linear and isotropic elastic behaviour of the material, the temperature changes according to the following equation (Oliferuk et al., 2012):

$$T_{k+1} = T_k - \frac{\alpha\, T_0\, \sigma_k}{\rho\, C_v} \tag{5}$$

In order to perform a quantitative analysis, the explicit incremental scheme (Forward Euler method) is applied (Eqs (6)–(9)) for the temperature integration, controlled with a constant value of the total strain increment, i.e. for temperature function given at the step k new values are determined at the step $k+1$ following given increment of the total strain (Skoczeń et al., 2014).

During the continuous plastic flow (stage 2, Fig. 16), the dissipated plastic power is converted (with some efficiency η) to heat, which is partly used to warm up the sample and partly exchanged by the convection between the sample and the surrounding liquid helium. The evolution of the temperature is calculated on the basis of the heat

balance equation:

$$T_{k+1} = T_k - \frac{\eta\,\sigma\,\Delta\varepsilon_k^p - \alpha\,T_0\,\sigma_k}{\rho\,C_v + \beta\frac{8}{g^2}\frac{\Delta\varepsilon}{V_\varepsilon}} \tag{6}$$

where β denotes thermal conductivity, g - thickness of the sample, $\frac{\Delta\varepsilon}{V_\varepsilon}$ - the estimated time increment, computed as the ratio of strain increment and strain rate.

The stage 3 of the serration (abrupt drop of the stress) takes place at the extremely short time (micro-seconds), hence, the heat exchange is neglected, and the total plastic power is converted to the heat and used for temperature increase. The heat balance therefore reads:

$$T_{k+1} = T_k - \frac{\eta\,\sigma\,\Delta\varepsilon_k^p - \alpha\,T_0\,\sigma^{serr}}{\rho\,C_v} \tag{7}$$

This equation describes the temperature peaks experimentally observed (Fig. 7).

During stage 4 (relaxation) there is no significant heat source and the sample is cooled down to the liquid helium temperature. The balance equation is written in the form:

$$T_{k+1} = T_k + \frac{\alpha\,T_0\,\sigma_k - \beta\frac{8}{g^2}\frac{\Delta\varepsilon}{V_\varepsilon}\,(T_k - T_0)}{\rho\,C_v} \tag{8}$$

The temperature decrement is calculated as long as the term in the parenthesis is greater than zero. The specific heat and the thermal conductivity in the above equations are the functions of the temperature, as shown in Fig. 3.

The results of numerical analysis are illustrated in Fig. 17. It is worth pointing out, that the proposed model assumes that the RVE travels together with the shear band. In other words, the thermometer moves during the displacement-controlled test along the specimen together with the shear band. Therefore, the peak values of the temperature produced by the model are almost constant (see Fig. 17), while the experimentally measured temperature has the comb-like profile (Fig. 5 c). However, the shape of the temperature function for a single serration is in good agreement with the experimental data (cf. Tabin et al., 2016).

For the high strain rate ($\dot{\varepsilon}_{304}^{\#1} = 0.06\ s^{-1}$) at 4.2 K the continuous plastic flow occurs. It means that the specimen achieved the temperature T_1 at the beginning of the test and serrations are not observed. (c.f. Temperature profiles in Figs. 15 (a) and Fig. 18 a). Therefore, the question is about the transition strain rate. Based on the presented numerical model it can be identified ($\dot{\varepsilon}_3 = 0.007\ s^{-1}$, Fig. 18 a). The model predictions are in good agreement with experimental results obtained during tension of austenitic stainless steels specimen at liquid helium (Ogata et al., 1985). The initially observed serrations gradually disappears. Therefore, based on the 1-D numerical model, the limits of the DPF can be calculated for austenitic stainless steels tested at 4.2 K (Fig. 18 c).

It is worth pointing out that for the high strain rate the heat generated during DPF is accumulated in the specimen from serration to serration, therefore the linear trend of temperature is observed (e.g. $\dot{\varepsilon}_2$, Fig. 18 a). It is important because the mechanical parameters of austenitic stainless steels significantly make worse after the transition from discontinuous to continuous is achieved (Obst and Nyilas, 1991; Ogata et al., 1985).

4. Discussion

There exist numerous experimental observations attesting to different hypotheses of DPF, however the question about their mechanism remained open until now (Pu et al., 2021; Pustovalov, 2008). The mechanical origin of plastic flow instability at 4.2 K in fcc materials is finally verified in this paper. It is worth pointing out that from the microscopical point of view it is possible to identify the individual mechanisms that participate during the plastic deformation in fcc materials at cryogenic temperatures. Nevertheless, the macroscopical response of the specimen is a resultant of all strain induced mechanisms, such as a plastic flow instability, a phase transformation, a geometry instability, a thermomechanical instability and a dynamic of dislocation pile-ups. Thus, for instance during the displacement-controlled uniaxial tensile test of austenitic stainless steel (dog bone specimen) at 4.2 K, the shear band occurs near to the specimen's shoulders (stress concentration effect). Then, the strain induced martensitic phase stabilizes the propagation of the shear band, leading to the significant Lüders-type strain, the high hardening and the quite large ductility of the ASS specimen at cryogenic temperatures. The SEM microstructure analysis of ductile fracture of 304 stainless steel specimen tested at 4.2 K was presented by Tabin et al. (2016).

In the Lüders range, the shear band develops across the specimen in the discontinuous and sequential way, which is reflected by the stress oscillation on the stress-strain curve (so called serrations) and the comb-like profile of the temperature. Each serration in stress-strain curve can be decomposed into 4 stages, each of them different in nature: elastic (1), plastic (2), abrupt drop of stress (3) and relaxation (4). These components are observed in the vast majority of experiments with austenitic stainless steels (Obst and Nyilas, 1991; Ogata and Ishikawa, 1986; Tabin et al., 2016). Moreover, each stage of the serration is accompanied by a considerable change of the temperature. Thus, during the elastic range (1) the drop of temperature occurs. It results from the elastocaloric effect. From the atomistic perspective, this effect is explained by the oscillation energy of the atom, the maximum kinetic energy is changed by the deformation, eventually, the partition of the oscillation energy is shifted by deformation, leading to a change in the time averaged kinetic energy and consequently to the drop of temperature (Fig. 15 a). Since thermodynamic parameters tend to zero when the temperature tends to 0 K, which causes the thermodynamic instability, the small changes of temperature can be monitored by thermistors. The increase of the temperature which occurs during the next stages of serration (2, 3) is related to the dissipation of the plastic power in the thermodynamic instability conditions. The experimental results testify that in Lüders range (stress plateau on stress-strain curve) the shear band propagates discontinuously from one end of the specimen to the other. This is reflected by the comb-like profile of temperature

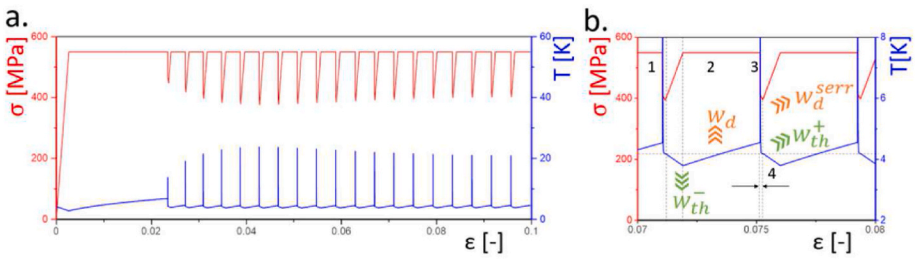

Fig. 17. a) Evolution of the stress σ (red) and temperature T (blue) as a function of strain ε during uniaxial tensile test of austenitic stainless steel (316 L) at 4.2 K; b) heat dissipation and absorption during single serration. (For interpretation of the references to colour in this figure legend, the reader is referred to the Web version of this article.)

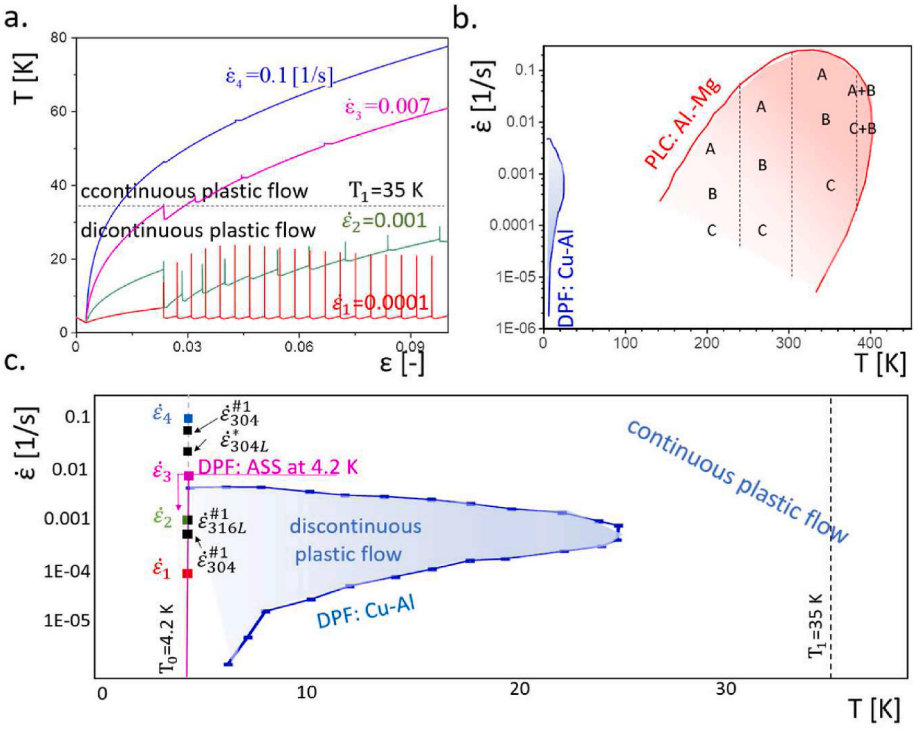

Fig. 18. Limits of plastic flow instability: a) temperature-strain curves in 316 L (numerical results) for different strain rate $(\dot{\varepsilon}_1, \dot{\varepsilon}_2, \dot{\varepsilon}_3, \dot{\varepsilon}_4)$, transition to continuous plastic flow; b)limits in strain rate-temperature space for Cu + 14 at.% Al (Dolgin and Natsik, 1991), (Zaiser and Hähner, 1997) and Al–Mg alloy, band types (A, B, C) corresponding to the PLC effect (Lebyodkin et al., 1997), (Ahmet, 2011); c) comparison between DPF limits for Cu+14 at.% Al (blue curve) and austenitic stainless steels (squares) - numerical results $(\dot{\varepsilon}_1, \dot{\varepsilon}_2, \dot{\varepsilon}_3, \dot{\varepsilon}_4)$ versus experimental one $(\dot{\varepsilon}^{\#1}_{304}, \dot{\varepsilon}^{\#1}_{316L}, \dot{\varepsilon}^{\#1}_{304}, \dot{\varepsilon}^{*}_{304L})$. For strain rate less than $\dot{\varepsilon}_3$ the serrations in austenitic stainless steel are observed. (For interpretation of the references to colour in this figure legend, the reader is referred to the Web version of this article.)

recorded by the thermometer. Such an effect can be used to identification of DPF origin. During special test, when the highest peak of the temperature occurs (the shear band was localized under the thermometer), the test is interrupted, and the specimen is unloaded (Fig. 8 a). Then, the specimen is loaded again. It turns out that the profiles of temperature and the stress are preserved. It can be concluded that the shear band develops in the active shear planes, and then propagates invariably through the specimen. It proves that the DPF is mechanically triggered. Nevertheless, the microstructure analysis for the different loading levels should give the in-depth explanation of the mechanisms observed during plastic deformation, both mechanically induced, as well as thermally activated.

It is worth pointing out that the experimental results confirm that DPF is coupled with strain induced fcc-bcc phase transformation. It results in the sequential and discontinuous shear band propagation in Lüders range (Fig. 7), and for a large strains the deformation is blocked by the martensitic phase, and the shear band is switched to another place until rapture occurs (Figs. 6 and 10). Therefore, the multiply necking pattern covered the 304 specimen after the uniaxial tensile test at 4.2 K. Such an effect was also observed in low C steel/304 austenite stainless steel laminates under tension at 77 K (He et al., 2020). In order to reduce severity of the strain concentration, the martensite phase was developed in the localized strain zone of 304.

The presented study shows that based on the time responses of the temperature and the elongation transducers, a full picture of the localized deformation behaviour can be obtained, including both spatial and temporal features. Moreover, for the displacement-controlled test, the velocity of the shear bands can be calculated in a simple way. The analysis was carried out for 304 and 316 L austenitic stainless steels. The experimental results show that the velocity in the Lüders-type strain range depends not only the strain rate (cf. Table 3), but also the chemical composition, the geometry of the specimen (Fig. 13) and the test conditions (cf. Cai et al., 2016). For a sufficiently high strain rate, the temperature of the specimen may increase even higher than transition temperature T_1. This, in turn, results in transition from the discontinuous to the classical plastic flow (Fig. 18 a). Based on the presented model the time responses of the thermometer for different strain rates are obtained. The model involves temperature effects driven by the elastocaloric effect and the plastic power dissipation. The DPF limits for ASS are determined and compered with the other fcc materials tested at wide range of temperature. It turns out, that at liquid helium temperature the transition strain rate for fcc materials reaches an approximate value independently from the specimen geometry (Fig. 18 c).

5. Conclusions

- The experimental results indicate that the DPF in fcc metals is mechanically triggered. During the displacement-controlled test of 316 L at 4.2 K, the unloading-loading test was carried out. Based on the time responses of transducers, the temporal and the spatial characteristics of the shear band in the Lüders range are determined. It turns out that when the specimen is once again loaded, the shear band continues propagation from the place where it has stopped before unloading.
- The new martensitic phase stabilizes the propagation of the shear band during the displacement-controlled uniaxial tensile test of ASS dog bone specimen at 4.2 K. It leads to the significant Lüders-type strain, the high hardening and the quite large ductility of the specimen at cryogenic temperatures.
- Based on the thermomechanical model of DPF, the limits of plastic flow instability in metastable austenitic stainless steels (e.g. 316 L) are obtained (the strain rate when transition temperature is achieved, and continuous plastic flow is observed, Fig. 18 a). The simulation results are in a great agreement with the experiment results.
- The elastocaloric effect is experimentally confirmed during the uniaxial tensile test of austenitic stainless steel at 4.2 K. The model of the temperature distribution during the DPF (Skoczeń et al., 2014) is extended to this effect.
- The rapture of the specimen takes place in accordance to the DPF - the serration pattern is maintained. Moreover, the DPF-induced crack jumps in CT specimen are observed (green curve on Fig. 12).

Author agreement statement

I the undersigned declare that this manuscript is original, has not been published before and is not currently being considered for publication elsewhere.

I confirm that the manuscript has been read and approved by author and that there are no other persons who satisfied the criteria for authorship but are not listed.

Data availability

The raw/processed data required to reproduce these findings can be shared with interested researcher upon reasonable request.

Declaration of competing interest

The Author declares that he has no known competing financial interests or personal relationships that could have appeared to influence the work reported in tis paper.

Acknowledgements

This work has been supported by the National Science Centre through the Grant No. UMO-2016/21/N/ST8/02368 and UMO-2017/27/B/ST8/00298. The author would like to thank Professor Błażej Skoczeń for the helpful discussions about the dissipative phenomenon at cryogenic temperatures. Also, I would like to thank Rafał Schmidt for the technical support.

References

Ahmet, Y., 2011. The Portevin–Le Chatelier effect: a review of experimental findings. Sci. Technol. Adv. Mater. 12, 063001.
Angel, T.H., 1954. formation of martensite in austenitic stainless steels. J. Iron Steel Inst. 177 (5), 165–174.
Basinski, Z.S., 1957. The instability of plastic flow of metals at very low temperatures. Proceed. Royal Soc. Lond. Ser. A 240, 229–242.
Bauer, P., Rajainmaki, H., Salpietro, E., 2007. EFDA Material Data Compilation for Superconductor Simulation. EFDA CSU, Garching.
Bertinelli, F., Fudanoki, F., Komori, T., Peiro, G., Rossi, L., 2006. Production of austenitic steel for the LHC superconducting dipole magnets. IEEE Trans. Appl. Supercond. 16, 1773–1776.
Brooks, J.W., Loretto, M.H., Smallman, R.E., 1979a. Direct observations of martensite nuclei in stainless-steel. Acta Metall. 27, 1839–1847.
Brooks, J.W., Loretto, M.H., Smallman, R.E., 1979b. Insitu observations of the formation of martensite in stainless-steel. Acta Metall. 27, 1829–1838.
Bućko, S., Jodłowski, H., Trzebicki, M., 2014. An experimental-numerical analysis of plastic zones initiation around holes in shields made of steel C45 under tension. Arch. Mech. Eng. LXI 179–198 nr 1.
Cai, Y.-L., Yang, S.-L., Fu, S.-H., Zhang, Q.-C., 2016. The influence of specimen thickness on the Lüders effect of a 5456 Al-based alloy: experimental observations. Metals 6, 120.
Chrysochoos, A., Martin, G., 1989. Tensile test microcalorimetry for thermomechanical behaviour law analysis. Mater. Sci. Eng.: A 108, 25–32.
Dolgin, A.M., Natsik, V.D., 1991. Criteria of instability and kinetics of jumps under unstable low temperature plastic flow. Acta Univ. Carol. Math. Phys. 32, 77–88.
Gao, S., Bai, Y., Zheng, R., Tian, Y., Mao, W., Shibata, A., Tsuji, N., 2019. Mechanism of huge Lüders-type deformation in ultrafine grained austenitic stainless steel. Scripta Mater. 159, 28–32.
Hallai, J.F., Kyriakides, S., 2011. On the effect of Lüders bands on the bending of steel tubes. Part I: Experiments. Int. J. Solid Struct. 48, 3275–3284.
Han, W., Liu, Y., Wan, F., Liu, P., Yi, X., Zhan, Q., Morrall, D., Ohnuki, S., 2018. Deformation behavior of austenitic stainless steel at deep cryogenic temperatures. J. Nucl. Mater. 504, 29–32.
He, J., Yuan, F., Yang, M., Zhou, L., Jiao, S., Wu, X., 2020. Exceptional tensile properties under cryogenic temperature in heterogeneous laminates induced by non-uniform martensite transformation and strain delocalization. Mater. Sci. Eng.: A 791, 139780.
Jin, H., Sanborn, B., Lu, W.Y., Song, B., 2021. Mechanical characterization of 304L-VAR stainless steel in tension with a full coverage of low, intermediate, and high strain rates. Mech. Mater. 152, 103654.
Kim, J.-H., Kim, S.-K., Lee, C.-S., Kim, M.-H., Lee, J.-M., 2014. A constitutive equation for predicting the material nonlinear behavior of AISI 316L, 321, and 347 stainless steel under low-temperature conditions. Int. J. Mech. Sci. 87, 218–225.
Lebyodkin, M., Dunin-Barkovskii, L., Bréchet, Y., Kubin, L., Estrin, Y., 1997. Kinetics and statistics of jerky flow: experiments and computer simulations. Mater. Sci. Eng.: A 234–236, 115–118.
Li, J., Zhou, Z., Wang, S., Mao, Q., Fang, C., Li, Y., Wang, G., Kang, J., Zhu, X., 2020. Deformation mechanisms and enhanced mechanical properties of 304L stainless steel at liquid nitrogen temperature. Mater. Sci. Eng.: A 798, 140133.
Liu, J., Kaoumi, D., 2018. Use of in-situ TEM to characterize the deformation-induced martensitic transformation in 304 stainless steel at cryogenic temperature. Mater. Char. 136, 331–336.
Marquardt, E.D., Le, J.P., Radebaugh, R., 2000. Cryogenic Material Properties Database, the 11th International Cryocooler Conference (Keystone, Co).
Murr, L.E., Staudhammer, K.P., Hecker, S.S., 1982. Effects of strain state and strain rate on deformation-induced transformation in 304 stainless steel: Part II. Microstructural study. Metallur. Trans. A 13, 627–635.
Nalepka, K., Skoczeń, B., Ciepielowska, M., Schmidt, R., Tabin, J., Schmidt, E., Zwolińska-Faryj, W., C, R., 2021. Phase Transformation in 316L Austenitic Steel Induced by Fracture at Cryogenic Temperatures: Experiment and Modelling (under review).
Obst, B., Nyilas, A., 1991. Experimental evidence on the dislocation mechanism of serrated yielding in f.c.c. metals and alloys at low temperatures. Mater. Sci. Eng.: A 137, 141–150.
Obst, B., Nyilas, A., 1998. Time-resolved flow stress behavior of structural materials at low temperatures. In: Advances in Cryogenic Engineering, vol. 44. Plenum Press, New York, pp. 331–338.
Ogata, T., Ishikawa, K., 1986. Time-dependent deformation of austenitic stainless steels at cryogenic temperatures. Cryogenics 26, 365–369.
Ogata, T., Ishikawa, K., Nagai, K., 1985. Effects of strain rate on the tensile behavior of stainless steels, copper, and an aluminium alloy at cryogenic temperatures. Tetsu-To-Hagane/J. Iron Steel Inst. Jpn. 71, 1390–1397.
Oliferuk, W., Maj, M., Litwinko, R., Urbański, L., 2012. Thermomechanical coupling in the elastic regime and elasto-plastic transition during tension of austenitic steel, titanium and aluminium alloy at strain rates from 10−4 to 10−1 s−1. Eur. J. Mech. Solid. 35, 111–118.
Park, W.S., Yoo, S.W., Kim, M.H., Lee, J.M., 2010. Strain-rate effects on the mechanical behavior of the AISI 300 series of austenitic stainless steel under cryogenic environments. Mater. Des. 31, 3630–3640.
Pobell, F., 2007. Matter and Methods at Low Temperatures. Springer, Berlin, Heidelberg, Germany.
Polatidis, E., Šmíd, M., Hsu, W.N., Kubenova, M., Capek, J., Panzner, T., Van Swygenhoven, H., 2019. The interplay between deformation mechanisms in austenitic 304 steel during uniaxial and equibiaxial loading. Mater. Sci. Eng.: A 764, 138222.
Pu, Z., Xie, Z.C., Sarmah, R., Chen, Y., Lu, C., Ananthakrishna, G., Dai, L.H., 2021. Spatio-temporal dynamics of jerky flow in high-entropy alloy at extremely low temperature. Phil. Mag. 101, 154–178.
Pustovalov, V.V., 2008. Serrated deformation of metals and alloys at low temperatures (Review). Low Temp. Phys. 34, 683–723.
Ren, S.C., Morgeneyer, T.F., Mazière, M., Forest, S., Rousselier, G., 2021. Effect of Lüders and Portevin–Le Chatelier localization bands on plasticity and fracture of notched steel specimens studied by DIC and FE simulations. Int. J. Plast. 136, 102880.
Rešković, S., Jandrlić, I., Vodopivec, F., 2016. Influence of testing rate on Lüders band propagation in niobium microalloyed steel. Metalurgija 55, 157–160.
Rossi, L., Sorbi, M., 2006. MATPRO: A Computer Library of Material Property at Cryogenic Temperature. CARE-Note-2005-018-HHH , Superconductors Database.
Seeger, A., 1957. Dislocations and mechanical properties of crystals. In: Fisher, J.J.C. (Ed.), An International Conference Held at Lake Placid. Wiley, New York.
Shibata, K., Ogata, T., Nyilas, A., Yuri, T., Fujii, H., Ohmiya, S., Onishi, T., Weiss, K.P., 2008. COMPARISON OF strength and serration at cryogenic temperatures among 304L, 316L and 310S steels. AIP Conf. Proceed. 986, 108–115.
Shibata, K., Ogata, T., Yuri, T., 2006. Effect of martensitic transformation on serration of 304L steel at cryogenic temperature. Adv. Cryog. Eng.: Trans. Int. Cryog. Mater. Conf. 52.
Skoczeń, B., 2004. Compensation Systems for Low Temperature Application. Springer-Verlag, Berlin.
Skoczeń, B., Bielski, J., Sgobba, S., Marcinek, D., 2010. Constitutive model of discontinuous plastic flow at cryogenic temperatures. Int. J. Plast. 26, 1659–1679.
Skoczeń, B., Bielski, J., Tabin, J., 2014. Multiaxial constitutive model of discontinuous plastic flow at cryogenic temperatures. Int. J. Plast. 55, 198–218.
Spencer, K., Véron, M., Yu-Zhang, K., Embury, J.D., 2009. The strain induced martensite transformation in austenitic stainless steels: Part 1 – influence of temperature and strain history. Mater. Sci. Technol. 25, 7–17.
Sun, H.B., Yoshida, F., Ohmori, M., Ma, X., 2003. Effect of strain rate on Lüders band propagating velocity and Lüders strain for annealed mild steel under uniaxial tension. Mater. Lett. 57, 4535–4539.
Suzuki, T., Kojima, H., Suzuki, K., Hashimoto, T., Ichihara, M., 1977. An experimental study of the martensite nucleation and growth in 18/8 stainless steel. Acta Metall. 25, 1151–1162.
Tabachnikova, E.D., Dolgin, A.M., Bengus, V.Z., Yefimov, Y.V., 1984. Fiz. Met. Metalloved. 58, 573.
Tabin, J., Prącik, M., 2015. Methods for identifying dynamic parameters of clip-on extensometer–specimen structure in tensile tests. Measurement 63, 176–186.
Tabin, J., Skoczen, B., Bielski, J., 2016. Strain localization during discontinuous plastic flow at extremely low temperatures. Int. J. Solid Struct. 97–98, 593–612.
Tabin, J., Skoczen, B., Bielski, J., 2017. Damage affected discontinuous plastic flow (DPF). Mech. Mater. 110, 44–58.
Tabin, J., Skoczen, B., Bielski, J., 2019. Discontinuous plastic flow coupled with strain induced fcc–bcc phase transformation at extremely low temperatures. Mech. Mater. 129, 23–40.

Tabin, J., Skoczeń, B., Bielski, J., 2021. Discontinuous plastic flow in stainless steels subjected to combined loads at extremely low temperatures. Int. J. Mech. Sci. 200, 106448.
Vorob'ev, E.V., 2006. New types of limit states of structural alloys related to the realization of the low temperature discontinuous yielding effect. Mechanics 57, 17–21.
Vorob'ev, E.V., Anpilogova, T.V., 2015. Kinetics of low-temperature discontinuous deformation of metals. Cryogenics 68, 59–66.
Vorob'ev, E.V., Anpilogova, T.V., 2013. Numerical analysis of the deformation instability of metals in liquid helium. Comput. Mater. Sci. 68, 66–72.
Wessel, E.T., 1957. Metals at low temperatures. Trans. ASM 49, 149.
Xin, J., Fang, C., Song, Y., Wei, J., Huang, C., Libeyre, P., Simon, F., Sgobba, S., 2017. Microstructure and mechanical properties of ITER correction coil case material. IEEE Trans. Appl. Supercond. 27, 1–7.
Yang, X.-S., Sun, S., Zhang, T.-Y., 2015. The mechanism of bcc α′ nucleation in single hcp ε laths in the fcc γ→hcp ε→bcc α′ martensitic phase transformation. Acta Mater. 95, 264–273.
Zaiser, M., Hähner, P., 1997. Oscillatory modes of plastic deformation: theoretical concepts. Phys. Status Solidi 199, 267–330.